This is the author's peer reviewed, accepted manuscript. However, the online version of record will be different from this version once it has been copyedited and typeset.

PLEASE CITE THIS ARTICLE AS DOI: 10.1116/6,0001483

Comparison of Single and Concentric Split-Ring Resonator Generated Microplasmas

Running title: SRR vs CSRR Microplasma

Running Authors: Dextre et al.

Andrew T. Walsten

University of Alabama in Huntsville, Mechanical and Aerospace Engineering Department, 301 Sparkman Dr, Huntsville, Alabama 35988.

Roberto A. Dextre

University of Alabama in Huntsville, Mechanical and Aerospace Engineering Department, 301 Sparkman Dr, Huntsville, Alabama 35988.

Kurt A. Polzin

NASA Marshall Space Flight Center, Advanced Concepts Office, Huntsville, Alabama 35808

Kunning G. Xua)

University of Alabama in Huntsville, Mechanical and Aerospace Engineering Department, 301 Sparkman Dr, Huntsville, Alabama 35988.

a) Electronic mail: gabe.xu@uah.edu

The microplasmas generated by a single split-ring resonator and a dual concentric split-ring resonator operating at the same frequency are compared. Argon is used as the working gas and held at a pressure of 0.5 torr. The surface electric fields in the resonators were simulated to gain insight into the behavior of the fields in each device. Double Langmuir probes were used to measure the plasma density and electron temperature in a 2-D plane 2 mm above the surface of the resonators. The single ring and the concentric ring resonators both had a maximum electron temperature in the discharge gap of 2.5 eV. The single and concentric split ring resonators had the same maximum measured plasma density of 1.19 \times 10¹⁷ m⁻³. Plots of the measured properties and comparisons with electric field simulations

PLEASE CITE THIS ARTICLE AS DOI: 10.1116/6.0001483

show the field coupling to the concentric ring and producing ignition in the secondary discharge gap. The concentric ring resonator has more spatially uniform temperature and density distributions relative to the single split-ring resonator.

I. INTRODUCTION

Microstrip resonators are comprised of thin conductive strips on high dielectric constant substrates. In certain geometric configurations, these resonators can produce microplasmas in a gas. A microplasma is a plasma where at least one physical dimension is confined to length scales of a millimeter or smaller. The small scale allows for the formation and sustainment of microplasmas at higher, non-vacuum pressures. Microplasmas, particularly at atmospheric pressures, have been studied for sterilization against bacteria^{1–4}, skin and tissue treatment^{5,6}, surface activation^{7,8}, nanomaterial synthesis^{9–11}, plasma metamaterials^{12,13}, and thin film coating ^{14,15}.

The goal of the present work is to compare the plasmas generated by a split-ring resonator (SRR) and a concentric split-ring resonator (CSRR) configuration at low pressures. Drawings of both devices are shown in Figure 1. In the SRR, microwave power is input at the SubMiniature version A (SMA) connection and propagates in both directions around the ring until reaching a physical gap. The gap is located such that the electric field vectors on either side of the gap have maximum amplitude but are in opposite directions, thereby creating a strong gap electric field capable of ionizing a gas. In the CSRR, an unpowered, electrically isolated concentric split ring is nested inside the outer powered ring, with the gap of the nested ring rotated 180° from the outer-ring gap. Microwave power

PLEASE CITE THIS ARTICLE AS DOI: 10.1116/6.0001483

from the outer ring couples with the inner ring, and in certain cases (low pressure, high power, close ring spacing) a second point of ionization at the inner-ring gap will form.

The generation of a plasma discharge in the isolated unpowered resonator ring due to electromagnetic coupling between the two resonators was first observed in linear resonator arrays^{16,17}. In those works, as the powered linear resonator was ignited, other unpowered resonators in proximity to, but electrically isolated from, the powered resonator also generated a plasma at their discharge gaps. This phenomenon propagated across an array of linear resonators resulting in ignitions at the gaps of multiple resonators. A disadvantage of this linear resonator array design is that the linear array structure produces weaker plasmas in resonators that are further from the powered resonator. The linear array is also less physically compact than ring resonators.

Research on CSRRs has generally focused on their novel magnetic response which allows them to be used as metamaterials. When used as metamaterials, CSRRs do not produce plasma, but instead can be used to produce electromagnetic properties that are not naturally occurring, such as left-handed materials or negative-index materials ^{18,19}. More recently, plasma generation in the unpowered secondary ring gap was been reported in experiments using a CSRR²⁰. In the circular geometry, the discharge gaps of the concentric inner rings are rotated 180° from the powered ring, allowing for the formation and bolstering of a single plasma volume versus the distributed plasma generated by linear arrays. This results in a CSSR producing a more uniform plasma on a length scale comparable to the diameter of the outer, powered ring. A compact, low power, and spatially uniform plasma source could have applications from materials processing^{21,22} to plasma metametials^{12,13,23} and in-space micropropulsion^{20,24,25}.

PLEASE CITE THIS ARTICLE AS DOI: 10.1116/6.0001483

Prevoius works has studied the effect of SRR size on the electron density and temeprature²⁴. In this work, the electron temperature and density in a SRR and CSRR are experimentally measured with double Langmuir probes to compare and quantify the effects of the second ring on basic plasma properties. Two-dimensional maps of temperature and density are plotted to show the spatial distribution of these properties and to compare the effects of the second ring on these properties. Ansys High Frequency Structure Simulator (HFSS) was also used to model the resonators and their electric fields, providing additional insight that was applied to the interpretation of the plasma measurements.

II. EXPERIMENTAL APPARATUS

A. SRR and CSRR Devices

Figure 1 shows a schematic of the SRR and CSRR designs. The resonators used in this work were fabricated on RT/Duroid 6010 laminate (relative substrate permittivity ϵ_r =10.2). The split rings were fabricated on one side of the substrate using wet etching techniques. The back plane of the substrate is masked and unmodified to serve as the ground plane. The outer powered ring size and configuration is the same for both the SRR and CSRR. The CSRR has an additional nested inner ring with the gap locations of the two rings offset by 180°. A small hole is drilled through the substrate at the location of the SMA connector. The central conductor of the connector is soldered to the ring and the connector shield is soldered to the back plane.

PLEASE CITE THIS ARTICLE AS DOI: 10.1116/6.0001483

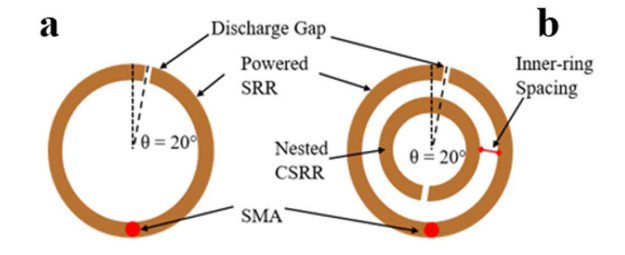


Figure 1. Schematic of (a) the SRR design and (b) the CSRR design.

The mean circumference l_{circ} of the outer powered ring is half the wavelength of the driving frequency f through the substrate, which is given as $l_{circ} = \frac{\lambda}{2} = \frac{c}{2f\sqrt{\epsilon_r}}$. Here, c is the speed of light and λ is the wavelength. As the microwaves propagate through the ring, a standing electromagnetic field is produced in the dielectric between the ring conductor plane and the ground plane. At the resonant frequency, the voltages on each side of the discharge gap are 180° out of phase as illustrated in Figure 2, resulting in a large amplitude electric field across the gap that ionizes the working gas. Successful operation of the resonator with a high gap field depends on gap placement, which is determined by the phase angle θ . In the CSRR, the additional nested ring should theoretically have a mean circumference that is sized to the first harmonic of the outer ring driving frequency so that both rings are operating in resonance. However, in practice this leads to a separation distance between the inner and outer rings that is too large for coupling to occur. Instead, the inner ring was designed so that the separation distance between the inner and outer ring was 1mm. This distance was chosen based both the limits of the fabrication process and on maximization of the electric field at both gaps as found with Ansys HFSS. The discharge

PLEASE CITE THIS ARTICLE AS DOI: 10.1116/6.0001483

gap in the nested ring is offset 180° from the outer ring discharge gap to maximize the volume of a plasma produced at the outer and inner ring gaps.

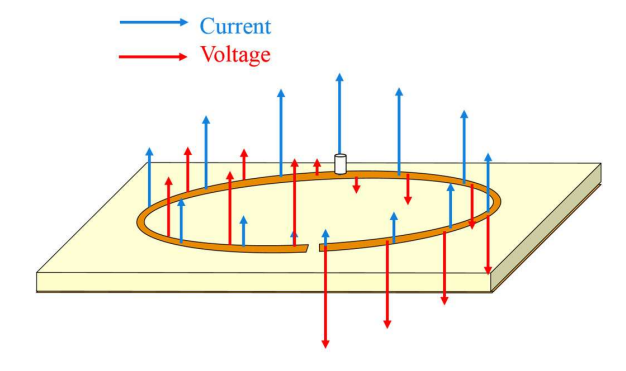


Figure 2. Schematic of current and voltage propagation in SRR.

The SRR and the outer ring of the CSRR share the same geometry for the ease of design and fabrication. The SRR was initially sized using common microstrip resonator equations^{24,26}, and then simulated and analyzed using Ansys HFSS to determine the frequency at which there would be a maximum electric field in the outer gap. For the CSRR, the same SRR geometry was used, but there are no theoretical equations readily available for design of the inner ring. Thus, the CSRR was designed entirely in Ansys HFSS using the SRR as the base. The phase angle and intra-ring spacing of the CSRR were adjusted in the simulation to maximize the gap electric fields for both rings.

A 500 μ m wide discharge gap was used for SRR and CSRR rings. All rings were designed with a strip width of 1.0 mm. The SRR was sized to be resonant at an input microwave frequency of 750 MHz while the CSRR was designed to have a separation distance of 1 mm from the outer ring. While theoretically designed for resonance at 750 MHz, prior experience has shown that the resonance in the fabricated devices tends to occur

PLEASE CITE THIS ARTICLE AS DOI: 10.1116/6.0001483

at higher frequencies. After fabrication, the real resonant frequency was experimentally determined by scanning the frequency and measuring the maximum forward power using a digital Bird power sensor. The experimentally determined resonant frequencies were 876 MHz for the SRR and 805 MHz for the CSRR. The larger shift in resonant frequency is possibly due to SRRs being able to be modeled as LC circuits^{27,28}. Larger capacitances lead to a decrease in the resonant frequency²⁷. The additional capacitance of the CSRR due to the addition of the second ring is possibly responsible for the larger resonant frequency of the SRR. Each ring was operated at its resonant frequency to achieve the optimum performance for more equal comparison.

B. Double Langmuir Probe

A double Langmuir probe was used to measure the electron temperature and number density of the generated plasma. The probe was fabricated from a 0.8 mm diameter double bore alumina tube holding two 0.1 mm diameter tungsten wires. The probe wire tips extend 1.5 mm beyond the alumina. The probe tip was located 2 mm above the surface of the resonators to measure the plasma. A two-axis Velmex stepper motor was used to sample a 2D grid and create maps of the plasma properties. The probe measured 81 separate points on a 9x9 grid as shown in Figure 3. Each step in the x- and y-direction was 2.54 mm. A 2400 Keithley sourcemeter was used to sweep the probe voltage from -30 V to 30 V and measure the resulting current.

PLEASE CITE THIS ARTICLE AS DOI: 10.1116/6.0001483

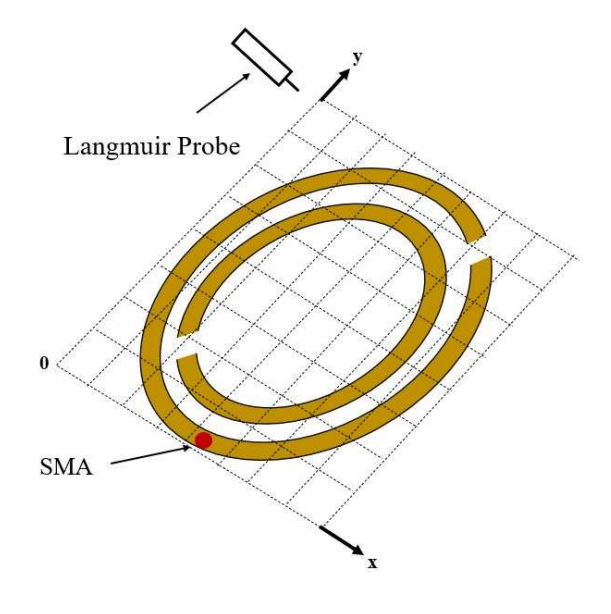


Figure 3. Sample Schematic of CSRR with gridded map showing points of current-voltage data acquisition.

The double Langmuir probe has both probe tips inserted into the plasma, with the tips biased relative to each other such that when there is a plasma present they form a complete circuit. When biased at high enough voltages, the current for one tip is limited by the ion saturation limit for the probe, which by current continuity also limits the electron current that can be collected by the other probe tip. This behaviour produces a symmetric I-V curve that passes ideally through I=0,V=0. In practice, the curve may be slightly asymmetric due to minor differences in the sizes of the two probe tips and the measured ion saturation current can continue to increase as a function of voltage due to sheath expansion. The detailed theory and derivation of the double Langmuir probe governing equations can be found in a number of references ^{29–31}. For the sake of brevity, only the final equations for calculating the electron temperature and plasma density are given here.

PLEASE CITE THIS ARTICLE AS DOI: 10.1116/6.0001483

The electron temperature, T_e is determined from the slope of the I-V curve evaluated at V=0,

$$\frac{kT_e}{e} = i_0 / \left(2 \frac{dI}{dV} \Big|_{V=0} \right) \tag{1}$$

where i_0 is the measured ion saturation current, $dI/dV|_{V=0}$ is the slope of the I-V curve evaluated at V=0, e is the elementary charge, and k is Boltzmann's constant. The Bohm criterion give the ion saturation current for a given probe size, electron temperature, and plasma density. Rearranging this to use the measured electron temperature and ion saturation current values to obtain the plasma density n_e yields

$$n_e = i_0 / \left[exp(-1/2) \ eA \sqrt{\frac{\kappa T_e}{m_i}} \right]$$
 (2)

where m_i is the ion mass and A is the probe surface area. Equation 1 assumes a symmetric I-V profile where the saturation current is the same for either leg. As this may not be true in practice, in this paper an average of the ion saturation current measurements for both legs is used in the analysis.

C. Facilities

A schematic of the experimental setup is shown in Figure 4. The SRR and CSRR were both operated at 876 MHz and 805 MHz respectively and achieved repeatable plasma ignition. A Hewlett Packard 8657b signal generator provided the microwave signal power. A +40 dB gain RF amplifier (RF Bay HPA-850) was used to increase the output power to achieve the desired input power. A Bird 7020 power sensor was used to measure the voltage standing wave ratio (VSWR) in the circuit. The sensor also measured the total

the online version of record will be different from this version once it has been copyedited and typeset

PLEASE CITE THIS ARTICLE AS DOI: 10.1116/6.0001483

This is the author's peer reviewed, accepted manuscript. However,

forward power to the devices, which was held at ~9 W for all experiments. Due to the different impedances of the SRR and CSRR, different VSWR values were obtained for each device at resonance, but similar forward power levels could be maintained in all cases. The devices were tested in argon at an ambient pressure of 0.5 torr as measured by a Baratron capacitance manometer. After successful microplasma generation, the device was allowed to operate for 5 minutes before Langmuir probe measurements were performed on the grid shown in Figure 3.

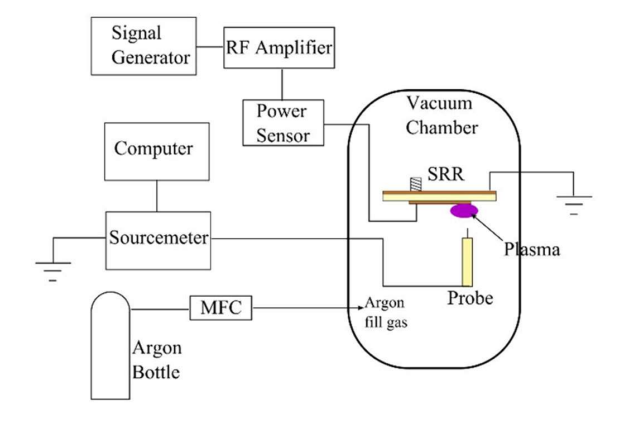


Figure 4. Diagram of the experimental setup.

III. HFSS Simulation Results

Before fabrication, the CSRR and SRR were both analyzed using Ansys HFSS. These simulations were all performed at thee reference design resonant frequency of 750 MHz to gain insight into how the rings in the CSRR electromagnetically couple and to quantify the effect of the intra-ring spacing between the outer ring and the electrically-isolated inner ring. As the outer ring of the CSRR is powered by the microwave signal, the

This is the author's peer reviewed, accepted manuscript. However, the online version of record will be different from this version once it has been copyedited and typeset.

PLEASE CITE THIS ARTICLE AS DOI: 10.1116/6,0001483

fringing electric fields of the powered ring couple to the nested ring^{32,33}, generating an electric field in the inner ring. This coupling produces a large electric field in the discharge gap of the nested ring.

The intra-ring spacing was varied in HFSS to determine the minimum and maximum coupling distance for the CSRR. Examples of the extreme cases where the intraring spacing was either too small or too large are shown in Figure 5. In the 2.0 mm spacing case of Figure 5 (left), there is no significant field within the nested ring. For the 0.1 mm spacing case in Figure 5 (right), the intra-ring spacing is too small, with the high electric field appearing not at the discharge gaps in the narrow space between the outer and the inner rings. It is important to note that the field strengths shown in Figure 5 are only on the conductor surfaces and not those in the discharge gaps. The field strengths in the gaps are extracted from the model by placing a working plane in those regions. The maximum gap field strengths are reported in Table 1 for for 0.1-2.0 mm intra-ring spacings. It is important to note that changing the separation distance of the two rings effects the resonant frequency. The resonant frequency for each simulation can be found by performing a frequency sweep over a large frequency range. Then, the reflection coefficient was plotted versus frequency. The frequency with the minimum reflection coefficient is the location of the resonant frequency. The electric fields given in Table 1 are based on operating each configuration at its specific resonant frequency. These data show the maximum outer and inner ring discharge gap electric fields occurs at an intra-ring spacing of 0.1 mm.

PLEASE CITE THIS ARTICLE AS DOI: 10.1116/6.0001483

E Field (V/m) a 1313758.88 1226238.38 1138718.00 1051197.50 963677.06 876156.63 788636.19 701115.69 613595.19 526074.75 438554.28 351033.81 263513.34 175992.86 951.93 b E Field (V/m) 479188.97 447248.94 415308.94 383368.91 351428.91 319488.88 287548.88 255608.86 223668.84 191728.83 159788.81 127848.80 95908.79 32028.76 88.75

Figure 5. Electric field in volts per meter along the surface of CSRRs with different intra-ring spacings (a) CSRR with 0.1 mm intra-ring spacing which causes interactions along circumference of the intra-ring spaces, and (b) CSRR with 2.0 mm intra-ring spacing showing no coupling to the nesting ring. Note the different color scales in the figures.).

Table 1. HFSS-simulated maximum discharge gap electric field intensities in volts per meter of both the powered and nested rings of a CSRR at 750 MHz for a range of intra-ring spacings.

Intra-Ring Spacing (mm)	Powered Ring peak (V/m)	Nested Ring Peak (V/m)
0.1	9.14×10^5	1.27×10^6
0.2	6.77×10^5	7.36×10^5
0.3	5.79 x 10 ⁵	4.14×10^5

PLEASE CITE THIS ARTICLE AS DOI: 10.1116/6.0001483

0.4	5.18×10^5	4.16×10^5
0.5	5.33×10^5	3.55×10^5
0.6	8.58×10^5	5.66×10^5
0.75	6.69×10^5	2.84×10^5
1.00	5.25×10^5	2.30×10^5
1.50	4.54×10^5	1.59×10^5
2.00	4.88×10^5	8.55×10^4

After the initial intra-ring spacing simulations were performed, the actual devices were tested. Though an intra-ring space of 0.1 mm appeared to have the maximum electric field, practical limitations in the wet etching fabrication process meant the minimum intra-ring spacing that could be reliably produced was 1 mm. The design resonant frequency, 750 MHz, was based on the operational range of the microwave amplifier. After fabrication the experimental resonant frequency for the CSRR was determined to be 805 MHz.

Electric field vector plots from simulations performed at resonance on the SRR and the CSRR with an intra-ring spacing of 1 mm are shown in Figure 6. These vector plots show the direction and relative magnitude of the local electric field along the rings. A standing wave pattern is established from one end of the discharge gap to the other. The opposing vectors at the discharge gaps produce a maximal change in electrical potential across the gap that causes ionization. Figure 7 shows the simulated conductor electric field intensities for the SRR and CSRR and shows the electric field intensity is maximized at the discharge gaps in both devices. Even though the outer ring geometries of the SRR and CSRR are the same, the CSRR has a stronger gap electric field in the outer ring. The maximum gap electric field is 5.00 x 10⁵ V/m for the SRR while for a 1 mm intra-ring

PLEASE CITE THIS ARTICLE AS DOI: 10.1116/6.0001483

spacing the CSRR has a maximum gap electric field of $5.25 \times 10^5 \text{ V/m}$ in the outer ring and $2.30 \times 10^5 \text{ V/m}$ in the inner ring. Figure 8 shows a photo of the operating SRR and CSRR, and visually there is a clear increase in plasma volume and intensity in the CSRR compared to the SRR.

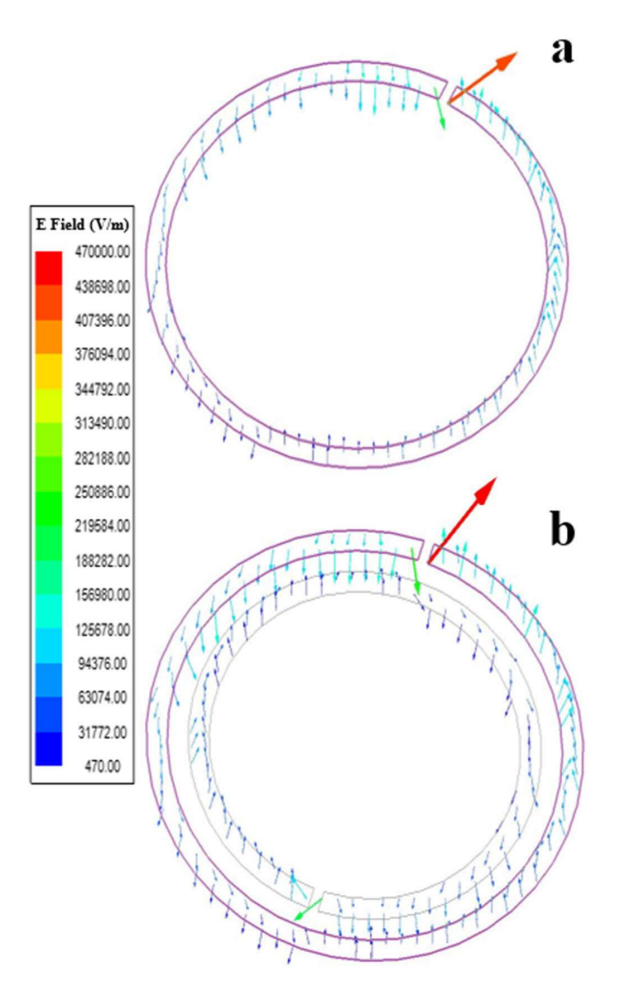


Figure 6. Electric field vector plots in volts per meter. (a) Single SRR vector plot at 750 MHz. (b) CSRR vector plot at 750 MHz and 1 mm intra-ring separation distance. The large red arrows correspond to the location of the maximum electric field at the gap.

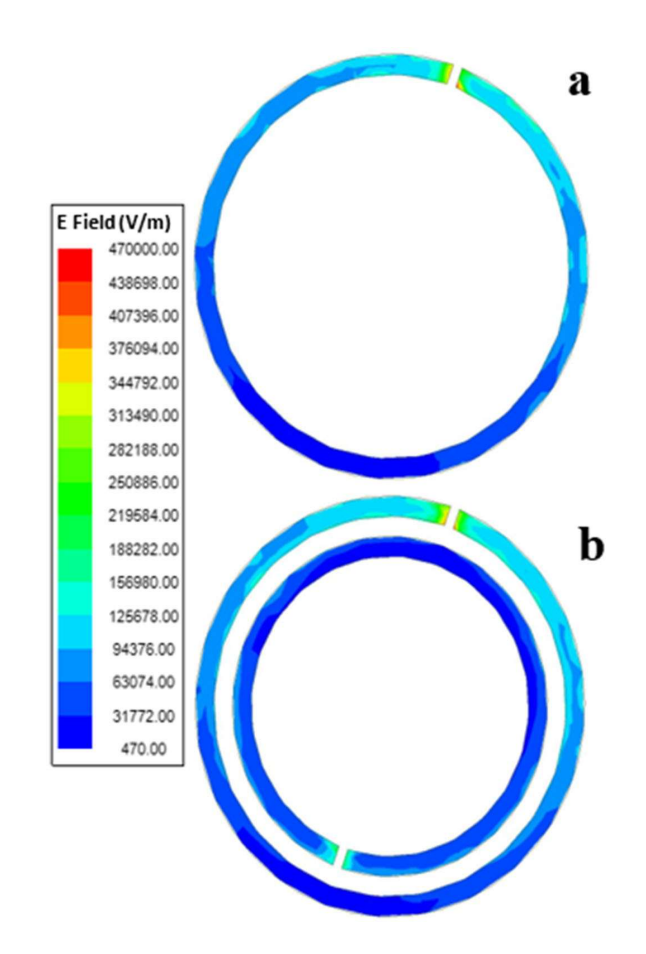


Figure 7. Magnitude of electric field in volts per meter along ring surface. (a) SRR Electric Field Intensity Simulation at 750 MHz. (b) CSRR Electric Field Intensity Simulation at 750 MHz.

This is the author's peer reviewed, accepted manuscript. However, the online version of record will be different from this version once it has been copyedited and typeset.

PLEASE CITE THIS ARTICLE AS DOI: 10.1116/6.0001483

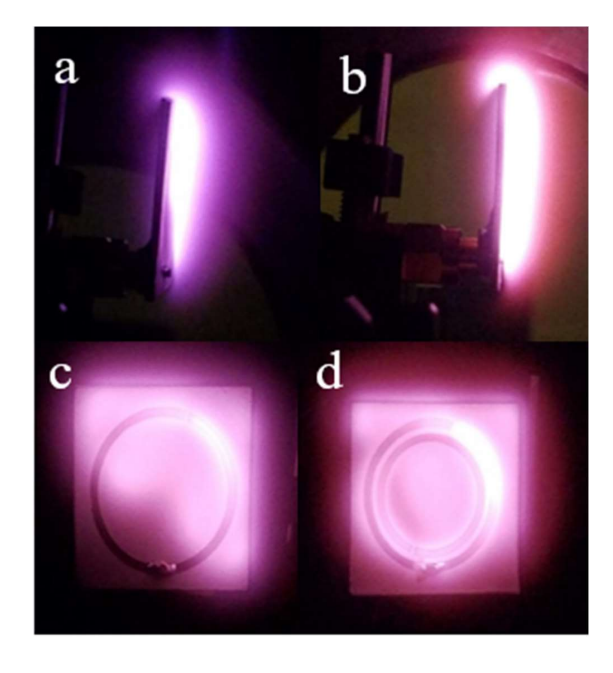


Figure 8. Photo of operating a) SRR side view, b) CSRR side view, c) SRR front view, and d) CSRR front view at ~9 W and 876 MHz and 805 MHz.

IV. Experimental Measurements

The experiments of the SRR and CSRR were done at their respective experimentally determined resonance frequency, which is higher than the calculated and simulated frequency.

A. Electron Temperature

The electron temperature measured at the 81 points of the 2D grid are plotted to create contour maps of the electron temperature. The countour maps are based on the average at each point for three separate days. The results for the SRR and CSRR are shown in Figure 9 and Figure 10, respectively. Dotted lines are added to the plots to indicate the discharge gap locations. In Figure 8, it can be seen that there is a lack a plasma near the edges and corners farthest from the outer rings gap. This is especially true for the SRR. It should be noted that the low density of the plasma affected the shape of the I-V curve at these

PLEASE CITE THIS ARTICLE AS DOI: 10.1116/6.0001483

locations and lead to large errors in the values within this region. This should be accounted for when considering this region. The SRR and CSRR plots show a mostly uniform temperature for the plasma except in the regions farthest from the outside gap. This region sees a sharp decrease in temperature and corresponds to the area with little to no plasma as observed in Figure 8. The second point of ionization of the CSRR leads to a larger volume of plasma which results in a larger area of uniform temperature over the CSRR. The uniformity of the SRR and CSRR's temperature can be attributed to the relativley short mean free path of the electrons. The mean free path can by found with $\lambda_m = 1/n_n\sigma$. The neutral density, n_n , can be found using the ideal gas law and the cross sections can be found from the NIFS database. For the given pressure and energy, the mean free path can be calculated to be approximately 2 mm. This is relatively small compared to the area of the SRR and leads to relatively fast thermalization of the plasma.

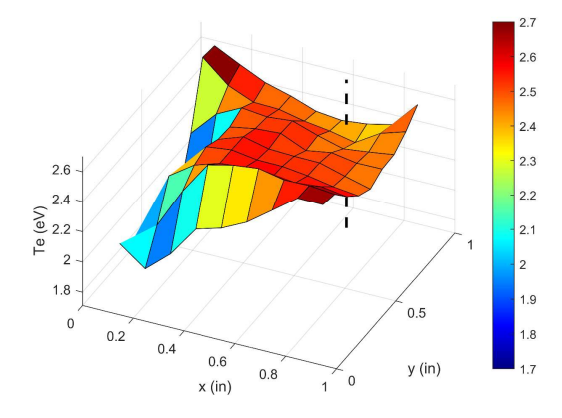


Figure 9. SRR Electron Temperature Distribution Contour Plot in eV at 876 MHz with 9 W of forward power.

PLEASE CITE THIS ARTICLE AS DOI: 10.1116/6.0001483

Figure 10. CSRR Electron Temperature Distribution Contour Plot in eV at 805 MHz with 9 W of forward power.

B. Plasma Density

Figure 11 and Figure 12 show the plasma number density contour plots for the SRR and CSRR, respectively. The maximum measured number density for both the SRR and CSRR is $1.19 \times 10^{17} \text{ m}^{-3}$. The average error on plasma density measurements is conservatively $\pm 21\%$ for the SRR and $\pm 12\%$ for the CSRR based on averages of multiple scans at each point. The large errors are largely do to the low plasma regions previously mentioned where densities were an order of magnitude lower than the regions of maximum density. Errors at each individual probe location ranged from 1% to 108% for the SRR and 1% to 62% for the CSRR.

The locations of maximum plasma density in both devices are spatially shifted clockwise from the outer gap. This can be explained by Figure 6 and Figure 7. The SRR simulation in Figure 7 has a maximum electric field at the gap, and the field is directed towards the right, or clockwise from the gap, as indicated by the red arrow. By comparison, the field is not as high in the conductor counterclockwise from the gap. This leads to more ionization clockwise of the gap. Through thermal diffusion, the density should decrease for

PLEASE CITE THIS ARTICLE AS DOI: 10.1116/6.0001483

points further from the region of high electric field, which is what we observed in the data sets presented in Figure 11 and Figure 12 and can be observed by the high intensity in the region in Figure 8. Figure 6 shows that the peak electric field at the gap points clockwise from the gap. Since probe measurements were acquired 2 mm above the surface, the plasma is shifted by the electric field. If measurements were acquired at the surface, it would be expected that the peak density would occur at the gap.

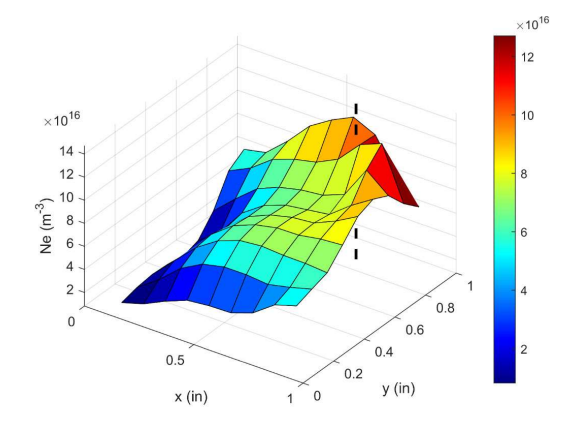


Figure 11. SRR Plasma Number Density Distribution Contour Plot in m⁻³ at 876 MHz with 9 W of forward power.

PLEASE CITE THIS ARTICLE AS DOI: 10.1116/6.0001483

×10¹⁶ 14 12 10 10 8 8 8 6 4 2 0 0.5 0.6 0.4 2 2 2

Figure 12. CSRR Plasma Number Density Distribution Contour Plot in m⁻³ at 805 MHz with 9 W of forward power.

Similar to the electron temperature profiles, the CSRR has a slightly more uniform density profile compared to the SRR. The discharge at the inner ring gap is an additional ionization source. The superposition of these two sources yields a net plasma that has a spatially-broader, more uniform density distribution relative to the SRR.

V. Conclusion

In this work, we presented plasma measurements for 0.5 torr argon microplasmas produced in an SRR and CSRR operated at an RF-frequency of 876 MHz and 805 Mhz with 9 W of forward power. Simulations of the electric field in the CSRR demonstrate that a microwave signal applied to the powered outer ring emits fields that couple into the inner nested ring. The simulations indicate that small intra-ring gaps (~0.1 mm) in a CSRR would yield maximum electrical coupling between the powered outer ring and the electrically-isolated inner ring and result in commensuratly high outer and inner ring

PLEASE CITE THIS ARTICLE AS DOI: 10.1116/6.0001483

discharge gap electric fields. Limitations on the manufacturing process forced the selection of a much larger 1 mm intra-ring gap spacing for our experiments. The measured maximum electron temperature and density in the SRR discharge gap were 2.5 ± 0.17 eV and 1.19 x $10^{17} \pm 21\%$ m⁻³, while the maximum values in the CSSR were 2.5 ± 0.14 eV and 1.19 x $10^{17} \pm 12\%$ m⁻³. Probe measurements clearly indicate a second point of ionization occurring at the discharge gap of the nested, unpowered ring in the CSRR. Compared to the SRR, the CSRR produced a plasma that was more uniform over a greater spatial region, both in terms of the measured electron temperature and density, but these data still exhibit significant maxima and minima in plasma density. These results suggest that the coupling behavior may be extensible to additional nested rings, which could be used to produce additional regions of ionization.

ACKNOWLEDGMENTS

This work was supported by the NSF EPSCoR RII-Track-1 Cooperative Agreement OIA-1655280 and the Adriel D. Johnson, Sr. Fellowship. Authors Walsten and Dextre would like to thank the support from the University of Alabama in Huntsville, the Mechanical and Aerospace Engineering Department, the Propulsion Research Center, and the Nano and Micro Devices Center for hosting the research and development of this microplasma source.

DATA AVAILABILITY

the online version of record will be different from this version once it has been copyedited and typeset.

PLEASE CITE THIS ARTICLE AS DOI: 10.1116/6.0001483

This is the author's peer reviewed, accepted manuscript.

The data that support the findings of this study are available from the corresponding author upon reasonable request. Email: gabe.xu@uah.edu

- ¹ K. Shimizu, M. Blajan, and T. Kuwabara, IEEE Trans. Ind. Appl. **47**, 2351 (2011).
- ² A. Mizuno, Int. J. Plasma Environ. Sci. Technol. **3**, 1 (2009).
- ³ S.K. Kang, Y.S. Seo, H.W. Lee, Aman-ur-Rehman, G.C. Kim, and J.K. Lee, J. Phys. D. Appl. Phys. 44, 435201 (2011).
- ⁴ K. Patel, A. Mannsberger, A. Suarez, H. Patel, M. Kovalenko, A. Fridman, V. Miller, and G. Fridmand, Plasma Med. **6**, 447 (2016).
 - ⁵ Y.C. Hong and H.S. Uhm, Appl. Phys. Lett. **89**, 221504 (2006).
- ⁶ K.-D. Weltmann and T. von Woedtke, Plasma Phys. Control. Fusion **59**, 014031 (2017).
 - ⁷ F. Fanelli and F. Fracassi, Surf. Coatings Technol. **322**, 174 (2017).
- ⁸ B.S. Tucker, P.A. Baker, K.G. Xu, Y.K. Vohra, and V. Thomas, J. Vac. Sci. Technol. A **36**, 04F404 (2018).
 - ⁹ H. Shirai, T. Kobayashi, and Y. Hasegawa, Appl. Phys. Lett. **87**, 1 (2005).
- ¹⁰ R.M. Sankaran, D. Holunga, R.C. Flagan, and K.P. Giapis, Nano Lett. **5**, 537 (2005).
- ¹¹ W.-H. Chiang, C. Richmonds, and R.M. Sankaran, Plasma Sources Sci. Technol. **19**, 034011 (2010).
- ¹² O. Sakai, T. Naito, T. Shimomura, and K. Tachibana, Thin Solid Films **518**, 3444 (2010).
 - ¹³ P.K. Singh, J. Hopwood, and S. Sonkusale, Sci. Rep. 4, 1 (2014).
- ¹⁴ J. Benedikt, V. Raballand, a Yanguas-Gil, K. Focke, and a von Keudell, Plasma Phys. Control. Fusion **49**, B419 (2007).
- ¹⁵ D. Merche, N. Vandencasteele, and F. Reniers, Thin Solid Films **520**, 4219 (2012).
 - ¹⁶ Z.-B. Zhang and J. Hopwood, Appl. Phys. Lett. **95**, 161502 (2009).
- ¹⁷ C. Wu, A.R. Hoskinson, and J. Hopwood, Plasma Sources Sci. Technol. **20**, 045022 (2011).
- ¹⁸ F. Bilotti, A. Toscano, and L. Vegni, IEEE Trans. Antennas Propag. **55**, 2258 (2007).
 - ¹⁹ P. Gay-balmaz, O.J.F. Martin, and I. Introduction, J. Appl. Phys. **92**, 2929 (2002).

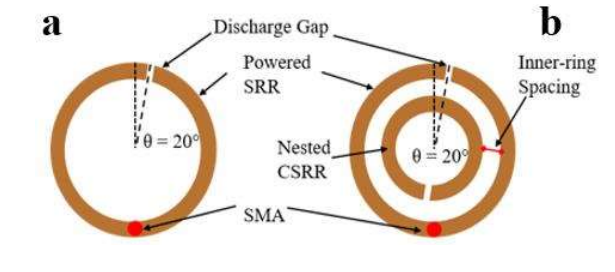
the online version of record will be different from this version once it has been copyedited and typeset.

This is the author's peer reviewed, accepted manuscript.

- ²⁰ R.A. Dextre, T. Yamauchi, K.A. Polzin, and K.G. Xu, IEEE Trans. Plasma Sci. **48**, 827 (2020).
 - ²¹ F. Iza and J. Hopwood, Plasma Sources Sci. Technol. 14, 397 (2005).
 - ²² F. Iza, S. Member, and J. a Hopwood, IEEE Trans, Plasma Sci. **31**, 782 (2003).
 - ²³ A. Iwai, Y. Nakamura, A. Bambina, and O. Sakai, Appl. Phys. Express **8**, (2015).
 - ²⁴ R.A. Dextre and K.G. Xu, **45**, 215 (2017).
- ²⁵ I. Levchenko, S. Xu, O. Cherkun, O. Baranov, and K. Bazaka, Adv. Phys. X **6**, (2021).
 - ²⁶ L. Changhong and L. Long, (2001).
 - ²⁷ C. Saha and J.Y. Siddiqui, Electromagnetics **32**, 345 (2012).
 - ²⁸ C. Saha and J.Y. Siddiqui, Int. J. RF Microw. Comput. Eng. 19, 615 (2009).
- ²⁹ F.F. Chen, in *Plasma Diagnostic Tech.*, edited by Richard H. Huddlestone and S.L. Leonard (Academic Press, New York, 1965).
 - ³⁰ P.M. Chung, L. Talbot, and K.J. Touryan, AIAA J. **12**, 144 (1974).
 - ³¹ B.A. Smith and L.J. Overzet, Rev. Sci. Instrum. **69**, 1372 (1998).
- ³² F. Iza, J.A. Hopwood, S. Member, and J.A. Hopwood, IEEE Trans. Plasma Sci. **31**, 782 (2003).
 - ³³ J. Hong and M.J. Lancaster, IEEE Trans. Microw. Theory Tech. **44**, 2099 (1996).

Journal of Vacuum Science Technology B

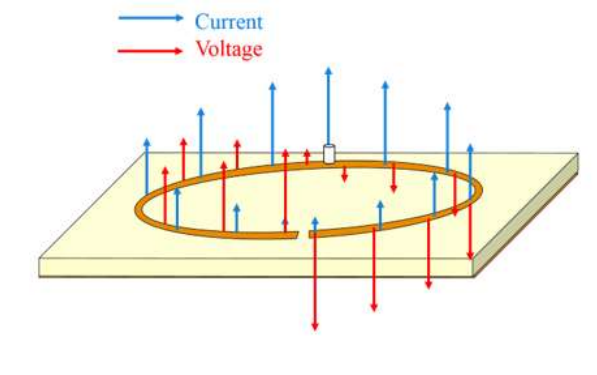






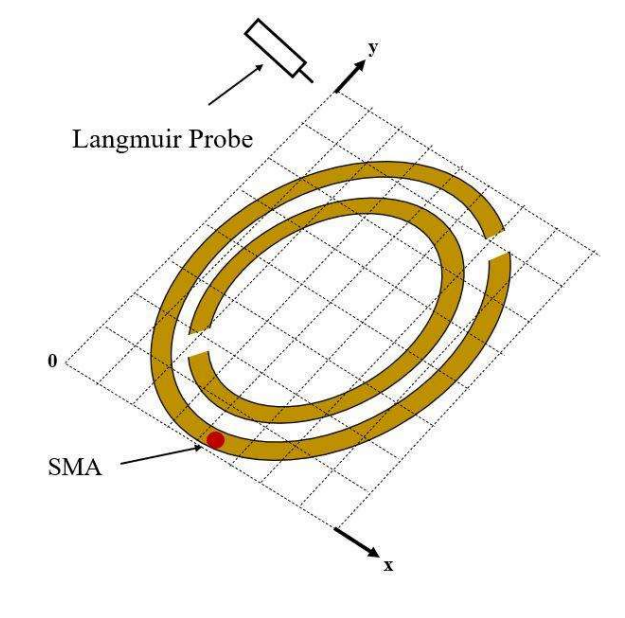






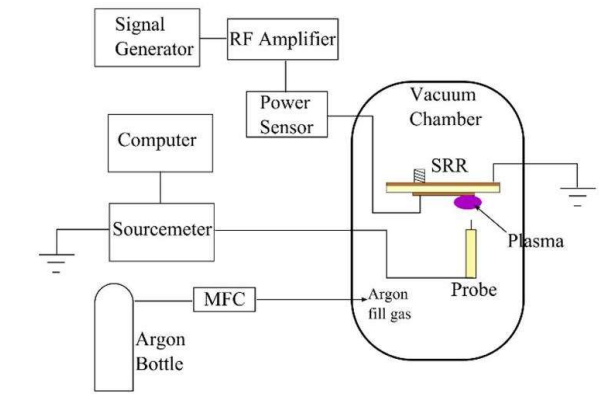
Journal of Vacuum Science Technology B





Journal of Vacuum Science Technology B

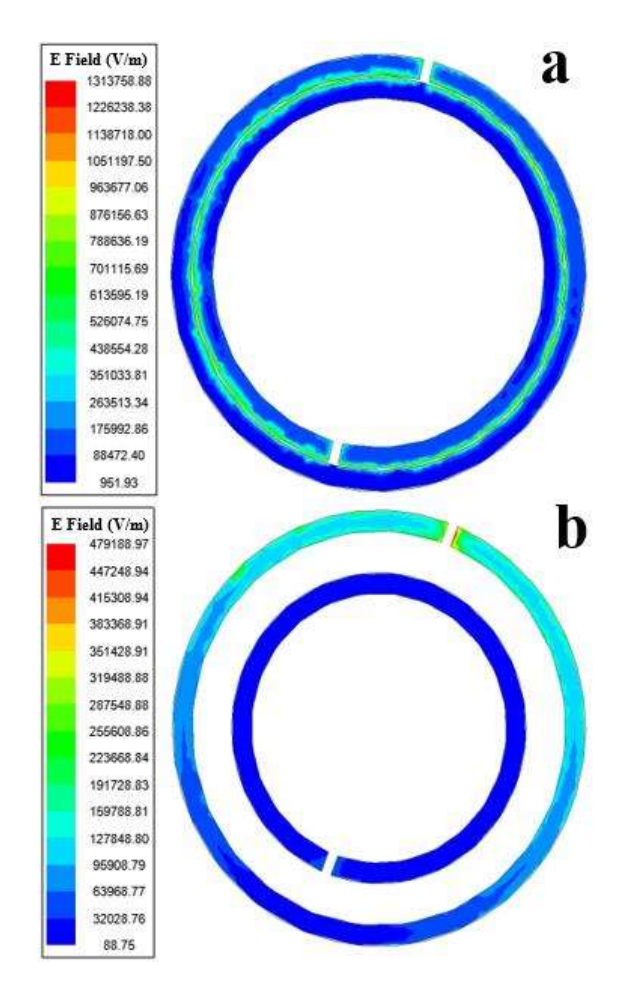




Journal of Vacuum Science Technology B



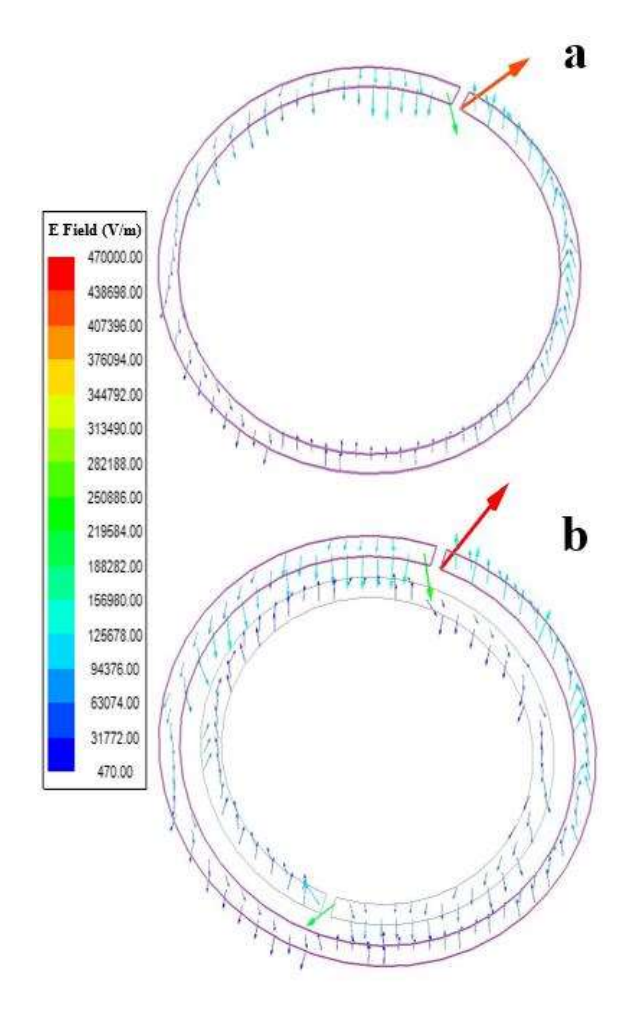




Journal of Vacuum Science Technology B



This is the author's peer reviewed, accepted manuscript. However, the online version of record will be different from this version once it has been copyedited and typeset. PLEASE CITE THIS ARTICLE AS DOI: 10.1116/6.0001483

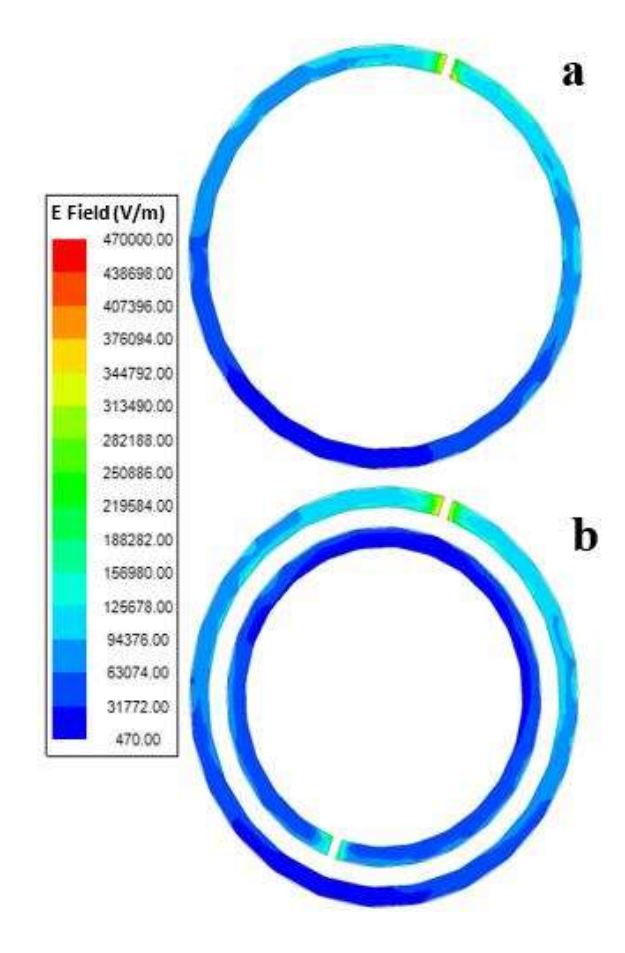


Journal of Vacuum Science Technology B



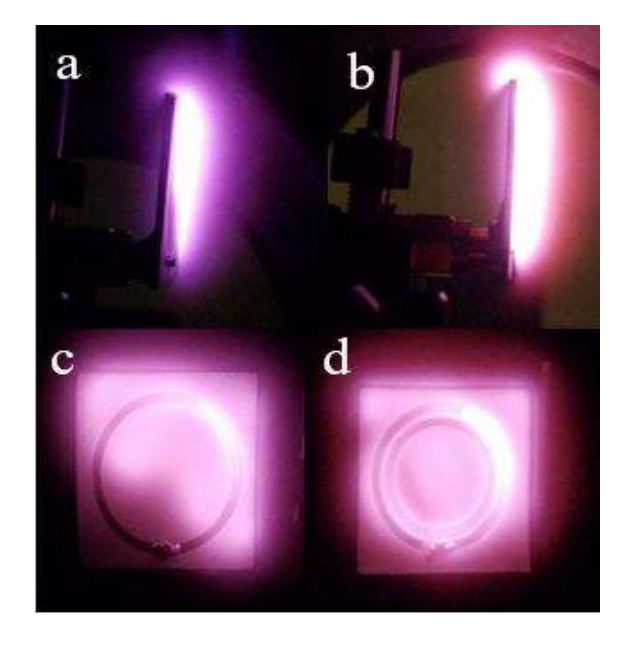
This is the author's peer reviewed, accepted manuscript. However, the online version of record will be different from this version once it has been copyedited and typeset.

PLEASE CITE THIS ARTICLE AS DOI: 10.1116/6.0001483



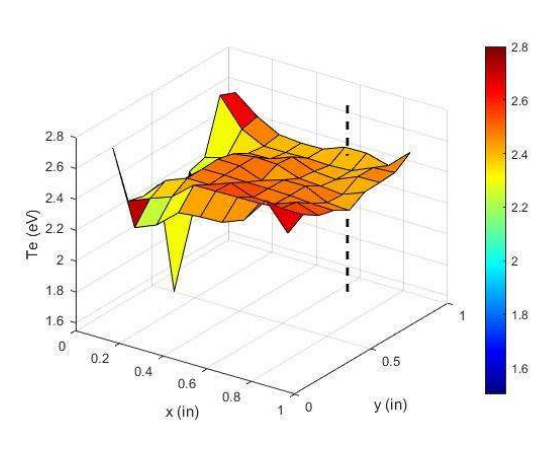


Journal of Vacuum Science Technology B



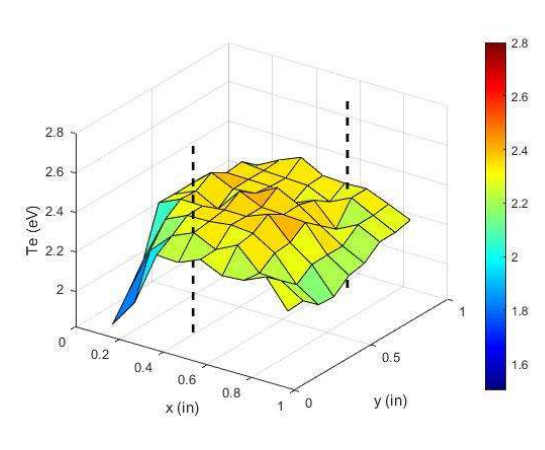


ACCEPTED MANUSCRIPT



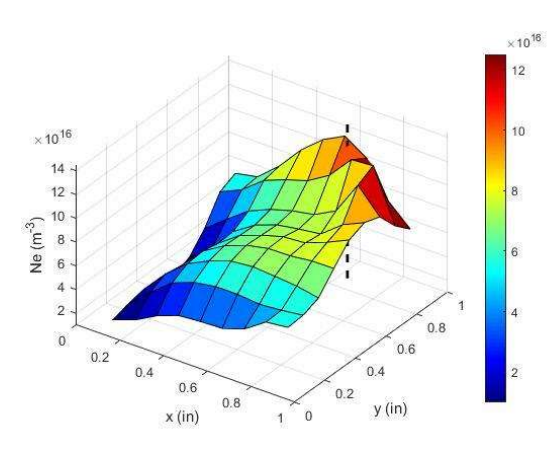


ACCEPTED MANUSCRIPT





ACCEPTED MANUSCRIPT





ACCEPTED MANUSCRIPT

